Electrochimica Acta 269 (2018) 479–489

Contents lists available at ScienceDirect

Electrochimica Acta

journal homepage: www.elsevier.com/locate/electacta

Cr-doped $Fe_2F_5 \cdot H_2O$ with open framework structure as a high performance cathode material of sodium-ion batteries

Min Liu, Xianyou Wang*, Shuangying Wei, Hai Hu, Rui Zhang, Lei Liu

National Base for International Science & Technology Cooperation, National-Local Joint Engineering Laboratory for Key Materials of New Energy Storage Battery, Hunan Province Key Laboratory of Electrochemical Energy Storage and Conversion, School of Chemistry, Xiangtan University, Xiangtan 411105, China

ARTICLE INFO

Article history:
Received 16 September 2017
Received in revised form
17 February 2018
Accepted 27 February 2018
Available online 6 March 2018

Keywords:
Sodium-ion batteries
Cathode material
Iron-based fluoride
Cr-doping
Electrochemical performance

ABSTRACT

The sphere-like $Fe_{(2-x)}Cr_xF_5 \cdot H_2O$ ($x = 0$, 0.03, 0.05, 0.07) composites with open framework structure are prepared via an IL based assisted approach, and served as the cathode material for Na-ion batteries (NIBs). The physicochemical and electrochemical properties of the Cr-doped $Fe_2F_5 \cdot H_2O$ cathode materials are systematically characterized. The results indicate that the Cr-doped materials not only reduce the crystalline size, but also remarkably enhance electronic conductivity. Meanwhile, the electrochemical tests further show that $Fe_{1.95}Cr_{0.05}F_5 \cdot H_2O$ as the cathode active material of NIBs exhibits a high initial discharge capacity of 357 mAh g^{-1} and retains a discharge capacity of 171 mAh g^{-1} after 100 cycles at 0.1 C (1 C = 200 mAh g^{-1}). Moreover, even at high rate of 1 C, it can still deliver a high discharge capacity of 147 mAh g^{-1}. Compared with the $Fe_2F_5 \cdot H_2O$, the $Fe_{1.95}Cr_{0.05}F_5 \cdot H_2O$ shows higher discharge capacity, excellent cycle stability and better rate capability, which can be attributed to the improvement of structure stability and electronic conductivity due to the appropriate amount (5%) of Cr^{3+} doping. Therefore, the preparation of Cr-doped $Fe_2F_5 \cdot H_2O$ sample provides a unique perspective to enhance the electrochemical performance of $Fe_2F_5 \cdot H_2O$, which is an essential step for the development of high specific energy sodium-ion batteries.

1. Introduction

Na-ion batteries (NIBs) are receiving the increasing attentions in electric vehicle, smart grid as well as other grid-scale energy storage systems (ESSs), due to its cost advantage, resource abundance and potentially better rate performance than lithium-ion batteries (LIBs) [1,2]. Besides, since the “rocking-chair” mechanism of the NIBs is similar to the LIBs, the accumulated knowledge and technology of LIBs promote the rapid development of NIBs. Until recently the layered transition metal oxide compounds, polyanion frameworks and prussian blue analogues (PBAs) have been extensively researched as NIBs cathode material candidates [3–6]. However, these cathode materials still expose some shortcomings, e.g., high hygroscopicity, narrow ionic channel and undesired phase transformation [7,8]. Fortunately, iron-based fluorides are competitive alternatives as sodium ion battery cathode materials owing to the large theoretical capacity and high operating voltage [9–11]. Among all fluorides, $Fe_2F_5 \cdot H_2O$ is the only case where the neutral and anionic clusters have a similar structure, and it can be classified as super halogens because of its high electron affinities (EAs) [12]. The Ferey group's study indicated that the $Fe_2F_5 \cdot H_2O$ pyrochlore is different from the normal hydrated pyrochlore where the H_2O molecules reside in the M_2X_6 network and can't be removed without damaging the open framework structure [13]. In addition, unlike the HTB phase, the $Fe_2F_5 \cdot H_2O$ pyrochlore phase does not exist Fe-F octahedral chains, and the corner-sharing of FeF_6 octahedral units are linked in a more random way to form a meandering ion channel, which provides enough space for electrolyte access and alleviates the volume expansion and multiphase interface generation during cycling process [14]. In our previous studies, since the unique open tunnel structure of the pyrochlore phase is more favorable for the transmission and storage of Na^+, a high discharge capacity has been obtained [15,16].

Despite its remarkable features as a promising candidate for NIBs, the wide band gap of Fe-F bonds leads a poor electronic conductivity, which leads to the low experimental capacity and fast capacity deterioration. Especially, it will produce multi-phase reaction in the electrochemical process (even in the insertion

* Corresponding author.
E-mail address: wxianyou@yahoo.com (X. Wang).

https://doi.org/10.1016/j.electacta.2018.02.159
0013-4686/

reaction phase), thus affecting its rate performance [17]. In order to address this limitation, most of the strategies have focused on the coating or modifying conductive layer on the surface of the materials and reducing size of particles. Chung's group [18,19] pyrochlore nano-particles inserted into the reduced grained graphene layer to form a FeF_3•$0.5H_2O$-rGO composite electrode, and obtained a sodium storage capacity of 266 mAh g^{-1} at 0.05 C. Li's group [20] reported the single-wall carbon nanotube (SWNT) wiring of FeF_3•$0.5H_2O$ as a cathode material for LIBs, which exhibited remarkable rate performance (220 mAh g^{-1} at 0.1 C and 80 mAh g^{-1} at 10 C). In addition, Jiang et al. [15,16] reported $Fe_2F_5 \cdot H_2O$ with reduced graphene oxide and the multi-wall carbon nanotubes wired $Fe_2F_5 \cdot H_2O$ particles as cathode materials of SIBs, which showed high initial discharge capacities of 251 mAh g^{-1} and 249 mAh g^{-1}, respectively. To a certain degree, the surface coating layer can reduce aggressive reaction between cathode electrode and organic electrolytes, and suppress the formation of a thick solid electrolyte interface (SEI). Nevertheless, the surface coating layer is usually too thin to provide a persistent protection against acidic species attack, leading to a slow capacity attenuation during charge/discharge process [21,22]. Accordingly, although the surface coating or modification can improve the surface electron conduction and Na ion migration rate, the Na ion mobility in bulk phase is still low. Recently, to improve the intrinsic electronic conductivity and electrochemical performance of iron fluoride, a small amount of high valence transition metal ions doping is considered as the significant route [23–25]. Among the various metals, Cr stands out as a promising candidate for effective doping element owing to its polyvalence and strong bond with nonmetalloid [26–28]. In addition, Cr^{3+}-doped metal fluorides have also been revealed good electrochemical performance [29], but it has never been studied in $Fe_2F_5 \cdot H_2O$.

In this work, the sphere-like $Fe_{(2-x)}Cr_xF_5 \cdot H_2O$ ($x = 0$, 0.03, 0.05, 0.07) composites with open framework structure are fabricated by an ionic liquid (IL) based assisted route. Since the doped Cr^{3+} ion (0.0615 nm) has a smaller ionic radius in octahedral coordination than that (0.078 nm) of Fe^{3+} and therefore its appropriate substitution of Fe sites can result in lattice defects, which not only reduces the particle size but also facilitates increased Na-storage activity, enhancing its discharge capacity and rate performance.

2. Experimental section

2.1. Preparation of $Fe_{(2-x)}Cr_xF_5 \cdot H_2O$ nanocomposites

All chemicals (analytically pure) were used without further purification. $Fe_{(2-x)}Cr_xF_5 \cdot H_2O$ ($x = 0$, 0.03, 0.05, 0.07) composites with open-structure are prepared by ionic liquid (IL) 1-butyl-3-methylimidazolium tetrafluoroborate ($BmimBF_4$), $Fe(NO_3)_3 \cdot 9H_2O$ and $Cr(NO_3)_3 \cdot 9H_2O$. The preparations of Cr-doped $Fe_2F_5 \cdot H_2O$ nanocomposites are schematically shown in Scheme 1. Firstly, 5 g $BmimBF_4$, used as a co-solvent, fluorine source and soft template, was dissolved in a round bottom flask in a 60 °C oil bath to obtain a uniform colorless solution. Then, $Fe(NO_3)_3 \cdot 9H_2O$ which provides an iron source and hydration water for $BmimBF_4$ hydrolysis, and $Cr(NO_3)_3 \cdot 9H_2O$ that severs as a Cr source, in molar ratios of 1.00:0, 0.97:0.03, 0.95:0.05 and 0.93:0.07 were gradually added in IL solvent, respectively, followed by continuous stirring at 60 °C for 12 h until the composite was completely precipitated. After cooling to room temperature naturally, in order to remove residual $BmimBF_4$, all products were washed with acetone and centrifuged at 8000 rpm five times. Finally, the prepared $Fe_{(2-x)}Cr_xF_5 \cdot H_2O$ composites were dried under at 90 °C for 36 h.

2.2. Materials characterization

The crystal structures of samples were characterized by X-ray diffraction (XRD, Rigaku D/MAX-2500 X-ray diffractometer) with Cu-Ka radiation. The material morphologies were investigated by scanning electron microscope (SEM, Nova NanoSEM230). Selected area electron diffraction (SAED) and transmission electron microscopy (TEM) measurements were carried out utilizing a transmission electron microscope (JEOL JSM-2100F). The atomic concentration and elemental distribution of the samples were verified by energy-dispersive X-ray spectroscopy (EDX JEOL JSM-6100LV). The oxidation state of elements in iron-based fluoride were checked by X-ray photoelectron spectroscopy (XPS, K-Alpha 1063) with an Al anode source.

2.3. Electrochemical measurements

The electrochemical performances of the $Fe_{(2-x)}Cr_xF_5 \cdot H_2O$ nanocomposites were measured in the CR 2025-type coin cells utilizing sodium metal as the counter electrode. The composite electrodes were prepared by mixing polyvinylidene fluoride (PVDF) binder, acetylene black (EC) and active material at a weight ratio of 1:1:8 in N-methyl pyrrolidione (NMP), with aluminum foil current collector, which were dried in vacuum at 110 °C for 24 h. The cells were assembled in an Ar-filled glove box. The cycling performances of the $Fe_{(2-x)}Cr_xF_5 \cdot H_2O$ nanocomposites were tested by charge-discharge measurement, where galvanostatic charge-discharge process was performed at various current densities in the voltage ranged from 1.0 to 4.0 V. Cyclic voltammograms (CV) and electrochemical impedance spectroscopy (EIS) were finished by a CHI604D electrochemical workstation. The CV tests were measured in the voltage ranged from 1.0 to 4.0 V at a scan rate of 0.2 mV s^{-1}. The frequency range of EIS was from 10^{-2}–10^5 Hz at potentiostatic signal amplitudes of 5 mV.

3. Results and discussion

In order to avoid the use of unsafe precursors such as HF and F_2, the synthesis of Cr-doped $Fe_2F_5 \cdot H_2O$ was performed by using a mildly hydrolyzable ionic liquid (IL) fluorination as the structure orientation and soft template function. The XRD patterns of $Fe_{(2-x)}Cr_xF_5 \cdot H_2O$ ($x = 0$, 0.03, 0.05, 0.07) nanocomposites are depicted in Fig. 1a. It can be observed that all characteristic diffraction peaks exhibit similarities, which match well with the standard peaks of $Fe_2F_5 \cdot H_2O$ (pyrochlore structure, Fd-3m-cubic space group, PDF No. 28–0483). Notably, no extra reflections were observed in the Cr-doped samples, which indicates that Cr element enters to the crystal structure of $Fe_2F_5 \cdot H_2O$ rather than forming impurities and does not vary its intrinsic crystal structure fundamentally. By the comparison of the (311) and (222) diffraction peaks, the diffraction peaks of Cr-doped $Fe_2F_5 \cdot H_2O$ nanocomposites shift slightly towards high degrees, which can be clearly observed in Fig. 1b. This is further proved that Cr is effectively doped in $Fe_2F_5 \cdot H_2O$. Additionally, the XRD patterns of $Fe_2F_5 \cdot H_2O$ and $Fe_{1.95}Cr_{0.05}F_5 \cdot H_2O$ were further analyzed by rietveld refinements, and the detailed results are presented in Fig. 1c–d. The lattice constants of the corresponding two materials are tabulated in Table 1. The reliability factor R_{wp} and χ^2 of the refinement are approximately 6.5% and 2.0, suggesting that the results are reliable. As being seen from Table 1, the lattice parameter (1.03986 nm) and unit cell volume (1.1244 nm^3) of $Fe_{1.95}Cr_{0.05}F_5 \cdot H_2O$ sample decrease slightly after Cr doping comparing with undoped $Fe_2F_5 \cdot H_2O$ (a = 1.04064 nm, Volume = 1.1269 nm^3) because the ionic radius of Cr^{3+} is slightly less than that of Fe^{3+}. Meanwhile, the atoms occupancy of the $Fe_2F_5 \cdot H_2O$ and $Fe_{1.95}Cr_{0.05}F_5 \cdot H_2O$ are given in Table 2. It can be

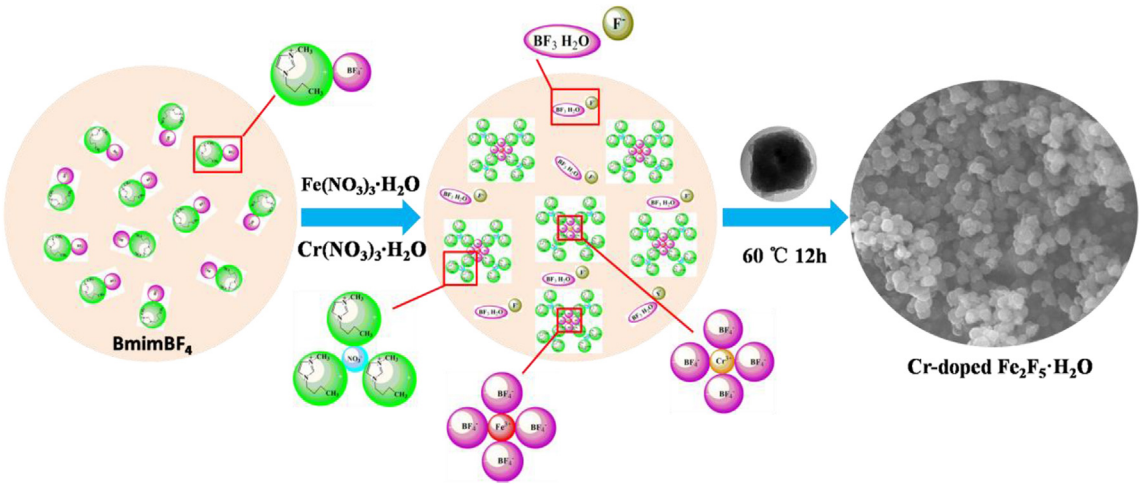

Scheme 1. Schematic diagram for the synthetic process of Cr-doped $Fe_2F_5 \cdot H_2O$ cathode materials.

found that Cr partially occupies the Fe (16c) site. Hence, the above results indicate that Cr-doping leads to a little crystal lattice contraction of $Fe_2F_5 \cdot H_2O$ but main crystal structure is not changed. In order to understanding the open framework structure in the crystal lattice, the crystal structure of $Fe_2F_5 \cdot H_2O$ is shown in Fig. 1e. In this typical face-centered cubic structure, six FeF_6 octahedra are connected one by one via sharing of vertex F atoms, resulting in the formation of a huge hexagonal cavity favorable for the storage of Na and electron transport, which are beneficial to achieve high discharge capacity [30]. The H_2O molecules reside within the cage made of the FeF_6 octahedra, stabilizing the frame skeleton. And the framework of the ligand can form a strong bond (such as hydrogen bonds), so that it is not easy to release from the skeleton and damage the pyrochlore structure.

The particle size and morphology of $Fe_{(2-x)}Cr_xF_5 \cdot H_2O$ nanoparticles can clearly be seen from the SEM images where all the samples have a sphere-like shape. Compared with the pure $Fe_2F_5 \cdot H_2O$ samples (Fig. 2a), a smaller particle size and pore size can be found after Cr-doping, as shown in Fig. 2b–d. As we all know, the smaller particle sizes of $Fe_{(2-x)}Cr_xF_5 \cdot H_2O$ samples will increase the specific surface areas and reduce efficiently the ion diffusion distances [25]. Furthermore, the particle surfaces of Cr-doped $Fe_2F_5 \cdot H_2O$ gradually become rough as the increasing Cr dopant amount, and some tiny particles adhere to the surface of the spherical particles, which is favorable for the electrolyte permeation and the enhancement of the electrochemical performances [24,31]. However, the size of sphere-like particle is not always reduced with the further increase of the amount of Cr doping. For example, when the Cr amount is higher than 5%, the particle size inversely increases. Notably, the $Fe_{1.95}Cr_{0.05}F_5 \cdot H_2O$ composite (Fig. 2c) with the appropriate amount of Cr-doping possesses the most uniform particle distribution size among all Cr-doped samples. The even distribution with the appropriate size of particles is beneficial for enhancing the electronic conductivity of $Fe_2F_5 \cdot H_2O$, which confers $Fe_{1.95}Cr_{0.05}F_5 \cdot H_2O$ better electrochemical performance than other materials [24].

As shown in Fig. 2e–f, the transmission electron microscopy (TEM) images of $Fe_{1.95}Cr_{0.05}F_5 \cdot H_2O$ sample reveals that the sphere-like particles (about 600 nm) consist of many primal grains approximately 10 nm in diameters that have the tendency to grow into much larger size particles with some large voids or tunnels. This structure allows the collection of free nanoparticles not only to increase the volumetric energy density of sodium batteries, but also to reduce the material damage resulting from volume expansion or structure collapses during cycling process. High-resolution transmission electron microscopy (HRTEM) image of the $Fe_{1.95}Cr_{0.05}F_5 \cdot H_2O$ nanocomposite is displayed in Fig. 2g. The measured lattice space of 0.31 nm can be well matched to (311) planes of the $Fe_2F_5 \cdot H_2O$. Meanwhile, the HRTEM image further confirms that a thin and amorphous protective layer approximately 2.96 nm is coated on the surface of the particle, which maybe helps to stabilize its structure and improve cycle stability [32]. Thus, Cr-doped $Fe_2F_5 \cdot H_2O$ with open framework structure can be significantly improved in terms of its performances.

To further investigate the element composition and distribution of the Cr-doped sample, in Fig. 2h the atomic ratios of Cr and Fe detected from the EDX spectrum are close to 1:19, which match well with the initial experimental data. In addition, the element mapping for the $Fe_{1.95}Cr_{0.05}F_5 \cdot H_2O$ sample for the two elements are presented in Fig. 2i, which suggest that Fe and Cr disperse evenly in the materials without phase separation. This indicates that $Fe_{1.95}Cr_{0.05}F_5 \cdot H_2O$ compound is well formed by the IL-based precipitation method.

The X-ray photoelectron spectroscopy (XPS) spectrum is illustrated in Fig. 3a–f to estimate the surface component and the elemental valence states of $Fe_{1.95}Cr_{0.05}F_5 \cdot H_2O$. The fitting lines are in different colors. It can be clearly seen from Fig. 3a that the peaks of C, O, F and Fe appear on the image while Cr is not observed obviously. It is probably because the Cr binding energy peak is disturbed and concealed by noise. As displayed in Fig. 3b, the spectrum of C 1s with a peak at 288.58 eV stems from the C-N bonding of the imidazolium ring of IL in Fig. 2g, which further confirms the presence of IL layer [32]. The binding energy at ~531.93 eV corresponds to the O1s peak (Fig. 3c), which may result from the H_2O molecules in the tunnel. On the other hand, a weak peak located at about 532.69 eV can be attributed to the hydration water that participate in the formation of the crystal structure [33,34]. As shown in Fig. 3d, the XPS spectrum of F 1s exhibits four peaks at 684.80, 685.0, and 685.99 eV, which can be assigned to FeF_2, FeF_3, and BF_4^+, respectively [32]. In addition, in Fig. 3e the Fe 2p spectrum of the $Fe_{1.95}Cr_{0.05}F_5 \cdot H_2O$ sample exhibits two contributions ($2p_{3/2}$ and $2p_{1/2}$), observed at respectively 713.98 and 727.44 eV, which can be corresponds to Fe^{3+}, while the obvious peaks located at 713.12 and 723.23 eV are ascribed to Fe^{2+} [35]. Thus, the above results suggest coexistence of Fe^{2+} and Fe^{3+} in the $Fe_{1.95}Cr_{0.05}F_5 \cdot H_2O$ material. In Fig. 3f, the binding energy values located at 578.49 and 588.27 eV demonstrate Cr ion in the +3 oxidation state [36,37], which further confirms that Cr has been

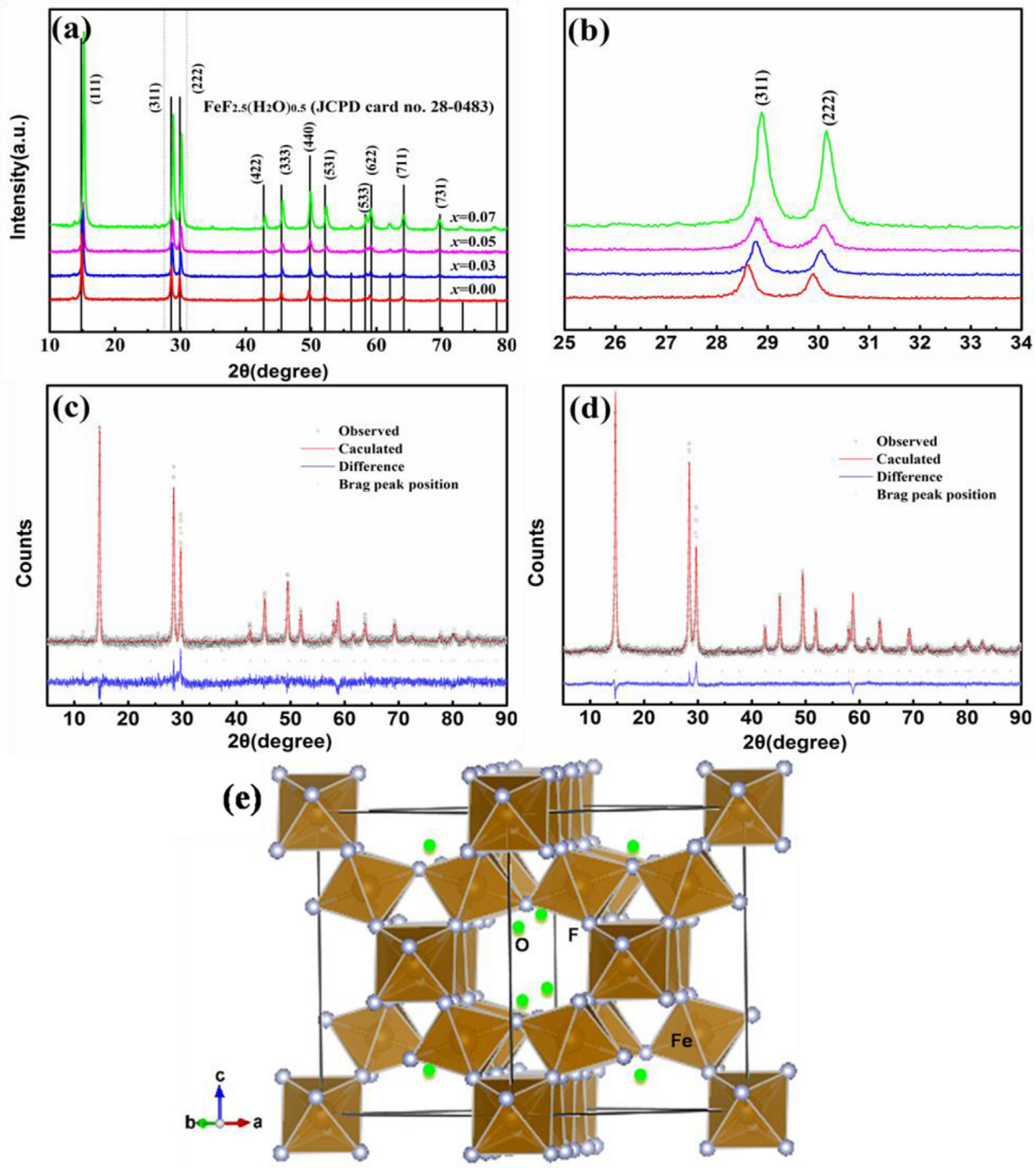

Fig. 1. (a) XRD patterns of $Fe_{(2-x)}Cr_xF_5 \cdot H_2O$ ($x = 0.00, 0.03, 0.05, 0.07$) nanocomposites. (b) Magnification of the (311) and (222) XRD peak. Rietveld refinement results of the X-ray diffraction patterns of (c) $Fe_2F_5 \cdot H_2O$ and (d) $Fe_{1.95}Cr_{0.05}F_5 \cdot H_2O$. (e) The crystal structure of $Fe_2F_5 \cdot H_2O$.

successfully doped into the lattice without changing the valence of Fe^{3+} and is in agreement with Rietveld refinement results of the XRD patterns.

To investigate the electrochemical performance of $Fe_{(2-x)}Cr_xF_5 \cdot H_2O$ ($x = 0$, 0.03, 0.05, 0.07) as the cathode for SIBs, the charge-discharge profiles of different cycles are recorded at 0.1 C, as presented in Fig. 4a–d. It can be clearly seen that all electrodes have two voltage plateaus in the first discharge curve of about 1.2 V and 2.5 V, whereas only one voltage plateau appears in the subsequent charge process and keeps about 2.5 V. In addition,

Table 1
Lattice parameters for $Fe_2F_5 \cdot H_2O$ and $Fe_{1.95}Cr_{0.05}F_5 \cdot H_2O$ crystals.

Sample	a (nm)	Volume (nm^3)	R_{wp}	R_p	χ^2
$Fe_2F_5 \cdot H_2O$	1.04064	1.1269	6.46%	4.83%	1.98
$Fe_{1.95}Cr_{0.05}F_5 \cdot H_2O$	1.03986	1.1244	6.71%	5.13%	2.21

Table 2
Structural parameters obtained from rietveld refinement of the XRD data for $Fe_2F_5 \cdot H_2O$ and $Fe_{1.95}Cr_{0.05}F_5 \cdot H_2O$.

Atom	Site	Occupancy	
		$Fe_2F_5 \cdot H_2O$	$Fe_{1.95}Cr_{0.05}F_5 \cdot H_2O$
Fe	16c	1.000	0.950
F	48f	1.000	1.000
O	8b	1.000	1.000
Cr	16c	1.000	0.050

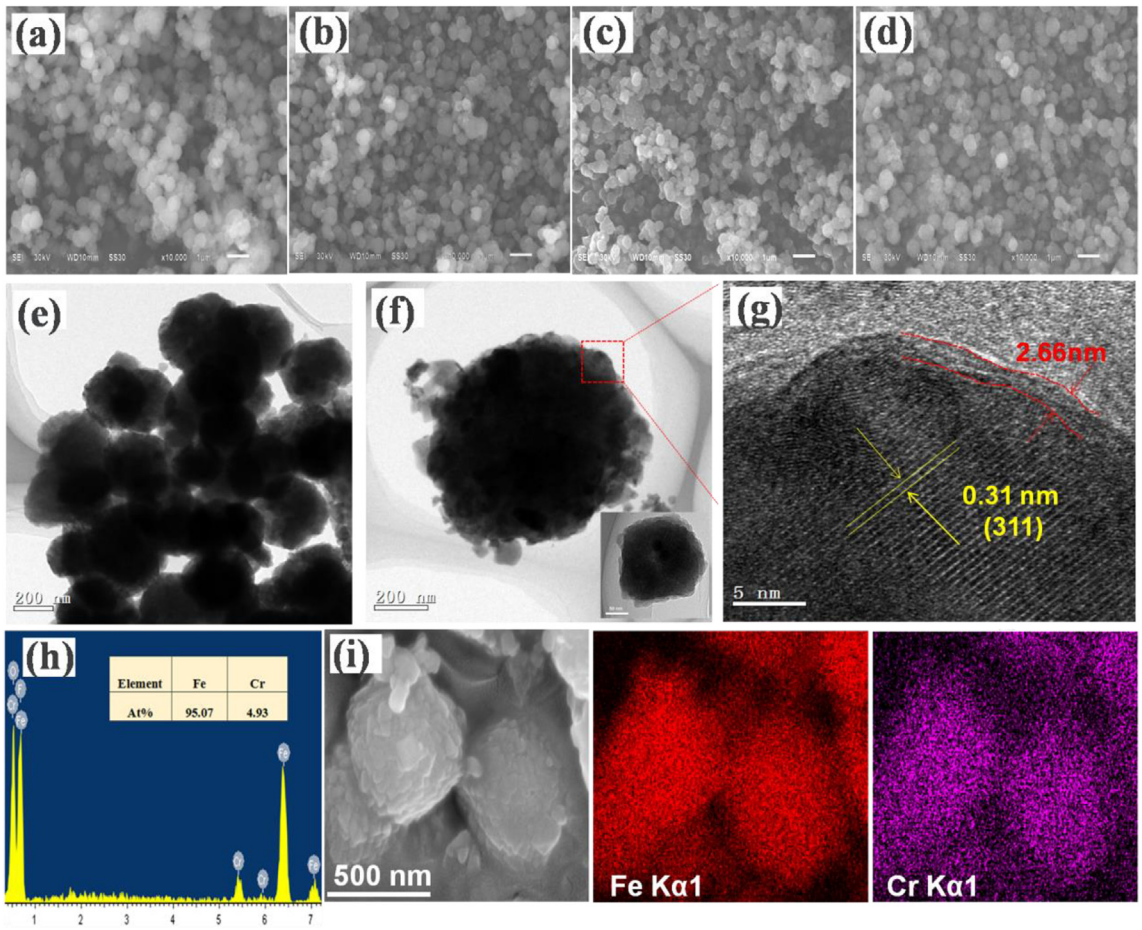

Fig. 2. SEM image of $Fe_{(2-x)}Cr_xF_5 \cdot H_2O$ (x=(a) 0.00, (b) 0.03, (c) 0.05, (d) 0.07) nanocomposites. ((e) and (f)) TEM and (g) HRTEM images of $Fe_{1.95}Cr_{0.05}F_5 \cdot H_2O$ nanocomposite. (h) The EDX spectrum of $Fe_{1.95}Cr_{0.05}F_5 \cdot H_2O$ nanocomposite. (i) SEM image and element mapping (Fe, Cr) of the $Fe_{1.95}Cr_{0.05}F_5 \cdot H_2O$.

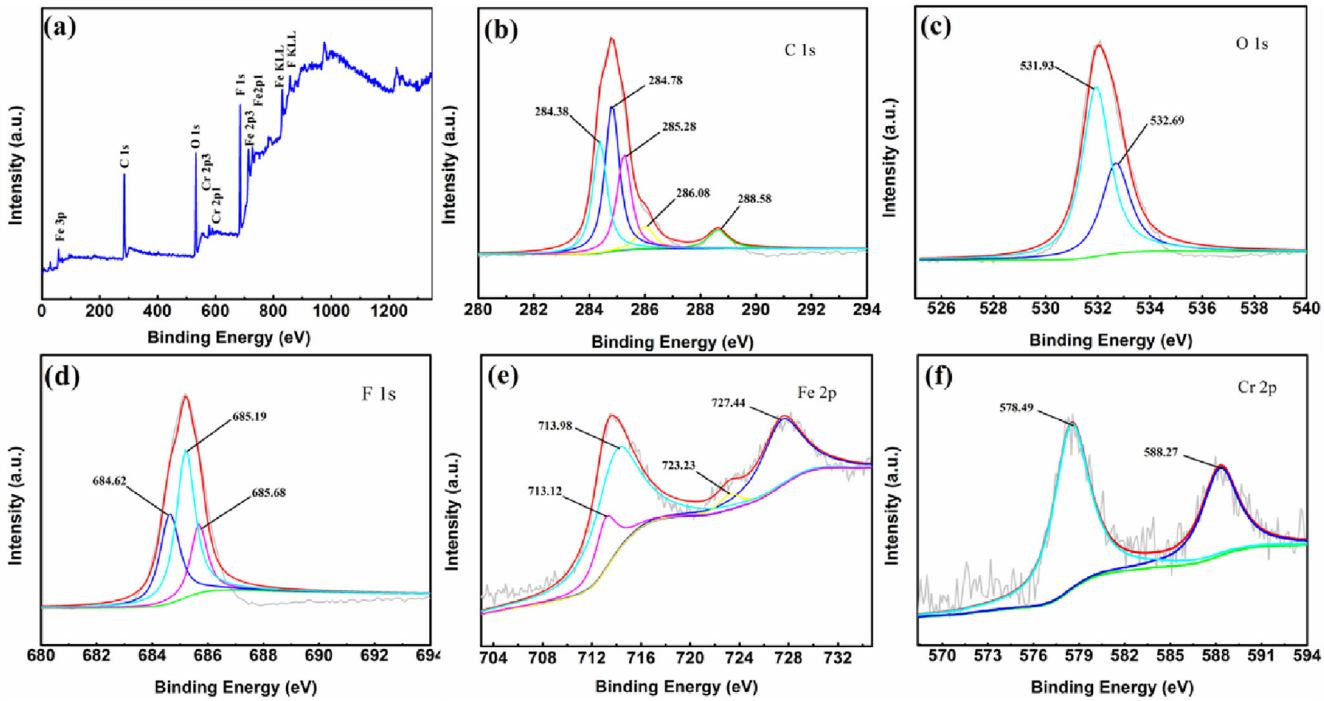

Fig. 3. XPS spectra of $Fe_{1.95}Cr_{0.05}F_5 \cdot H_2O$ nanocomposite: (a) survey spectrum and core-level spectra of (b) C1s, (c) O1s, (d) F1s, (e) Fe2p and (f) Cr2p.

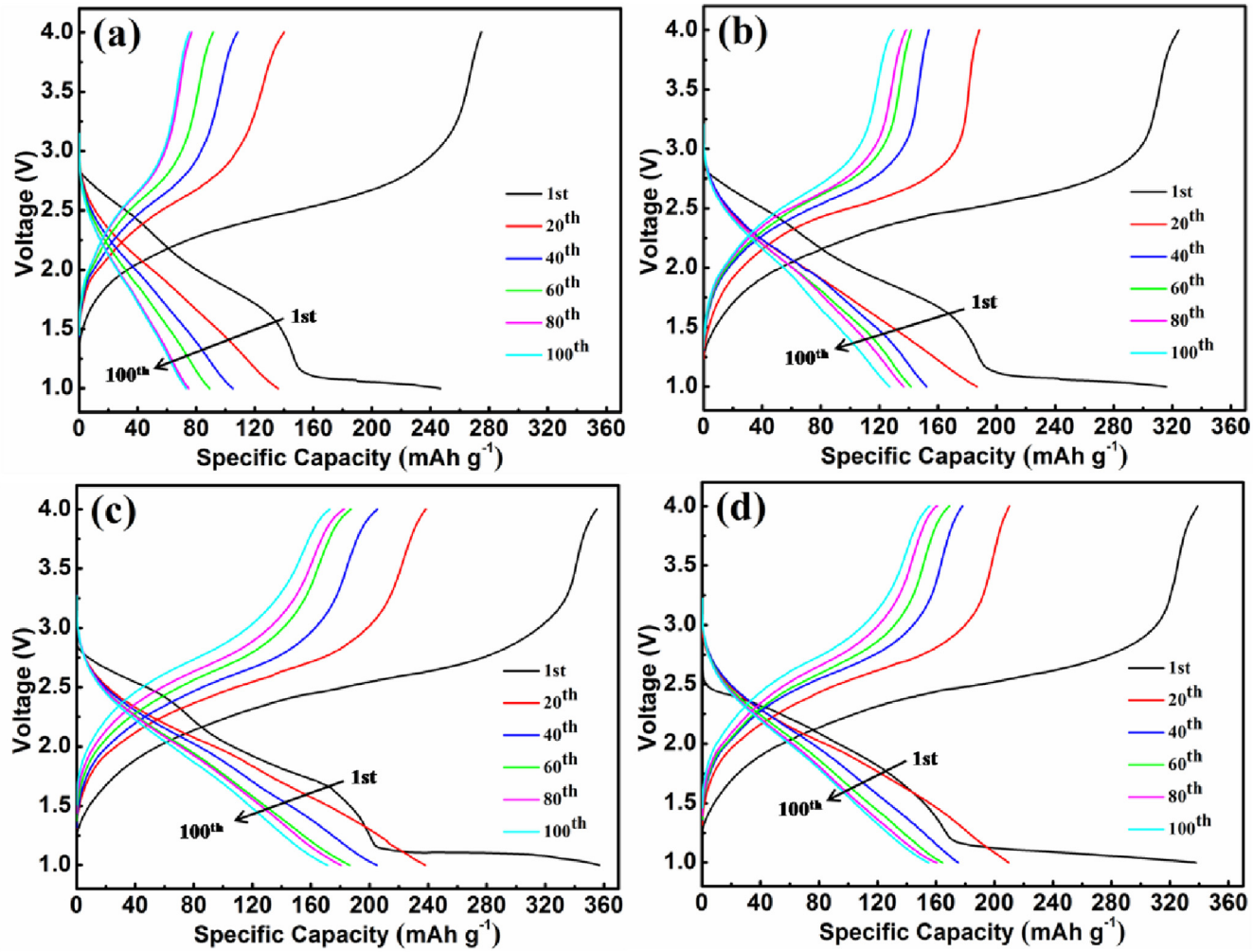

Fig. 4. Discharge and charge profiles of (a) $Fe_2F_5 \cdot H_2O$, (b) $Fe_{1.97}Cr_{0.03}F_5 \cdot H_2O$, (c) $Fe_{1.95}Cr_{0.05}F_5 \cdot H_2O$ and (d) $Fe_{1.93}Cr_{0.07}F_5 \cdot H_2O$ composite at 0.1C at different cycles (1st, 20th, 40th, 60th, 80th, and 100th).

$Fe_{1.93}Co_{0.07}F_5 \cdot H_2O$ electrode exhibits the highest discharge voltage plateau and lowest charge voltage plateau from the first to the 100^{th} cycles, which suggests that it has the smallest electrochemical polarization and thus can mitigate the voltage hysteresis. Compared to the bare $Fe_2F_5 \cdot H_2O$ with a low initial discharge capacity of 247 mAh g^{-1}, the Cr-doped samples exhibit relatively higher discharge capacity, which can be assigned to the increase of the electronic conductivity after Cr doping. The initial discharge capacities when $x = 3\%$, 5%, 7% are 316, 357, and 338 mAh g^{-1}, respectively. Obviously, the appropriate amount of Cr-doping will be favorable for increasing specific capacity, but the 7% Cr-doping shows an opposite result.

However, at second cycle, the discharge capacities of $Fe_{(2-x)}Cr_xF_5 \cdot H_2O$ ($x = 0$, 0.03, 0.05, 0.07) materials decreased to 205, 250, 299 and 272 mAh g^{-1} (Fig. 5a), respectively. This phenomenon is related to the irreversible formation of solid electrolyte interphase (SEI) [38–42]. And it is interesting to note that, within a certain range, the initial capacity loss decreases as the Cr dopant concentration increases. Until the 100^{th} cycle, the discharge capacity of bare $Fe_2F_5 \cdot H_2O$ rapidly reduces to 73 mAh g^{-1}, which is merely 29.6% of the first discharge capacity. The discharge capacities of $Fe_{(2-x)}Cr_xF_5 \cdot H_2O$ ($x = 0.03$, 0.05, 0.07) samples at 100 cycles maintains 127, 171, and 155 mAh g^{-1}, respectively. Apparently, the cycling stability is significantly improved after Cr-doping and the capacity retentions increase along with the increasing Cr dopant concentration. Besides, it can be clearly seen that the Coulombic Efficiencies (CEs) of Cr-doped materials are as high as 98% and obviously higher than pure $Fe_2F_5 \cdot H_2O$ at the beginning. As previously mentioned, the crystalline size increases as the doping amount of Cr increases (still smaller than the size of pure $Fe_2F_5 \cdot H_2O$), resulting in the reduced specific surface area. In general, the smaller the specific surface area is, the less favorable the specific capacity is, which has been proved by the low specific capacity of $Fe_{1.93}Cr_{0.07}F_5 \cdot H_2O$ nanocomposite. However, a smaller specific surface can help suppress side effects and inhibit SEI formation, which produces good reversible capacity in the second cycles and high CE. In short, although the $Fe_{1.93}Co_{0.07}F_5 \cdot H_2O$ exhibits the best cycling performance, its specific capacity is much lower than that of $Fe_{1.95}Co_{0.05}F_5 \cdot H_2O$, which is caused by the overgrowth of the microcrystal as mentioned above. Compared with other two composites, $Fe_{1.95}Co_{0.05}F_5 \cdot H_2O$ shows an excellent cycling performance and delivers the highest specific capacity, which is attributed to the increased electronic conductivity owing to proper Cr-doping as well as to the favorable porous morphology with nano-sized grains of the active material [27].

To further illustrate the effects of Cr-doping on the rate capacities of $Fe_{(2-x)}Cr_xF_5 \cdot H_2O$ ($x = 0$, 0.03, 0.05, 0.07) compounds, Fig. 5b gives the discharge performances at various current densities (0.1, 0.2, 0.4 and 1 C) for 5 cycles. As being seen, all materials display a relatively low specific capacity due to the increase of current

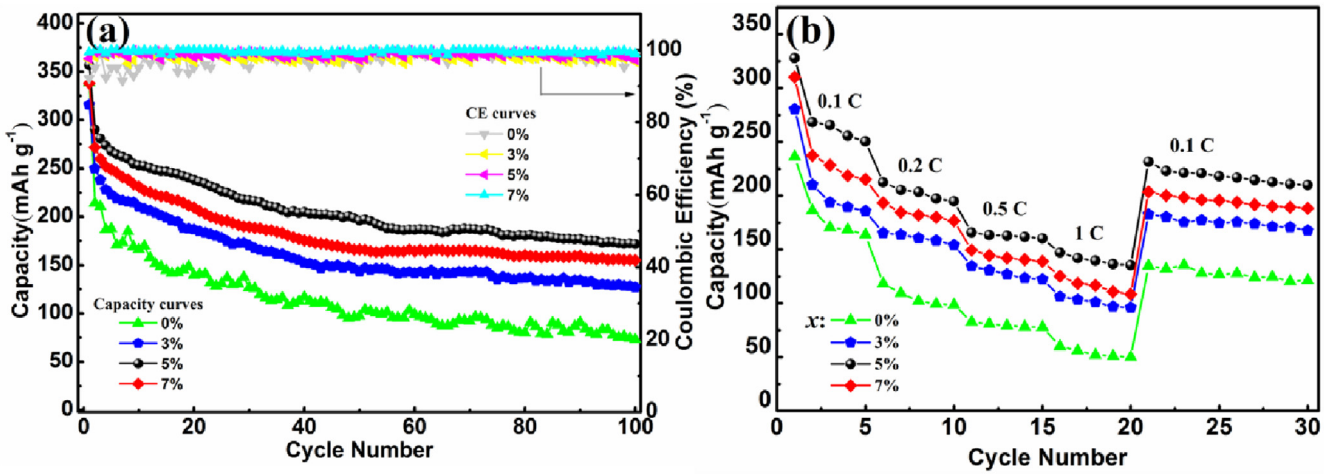

Fig. 5. (a) Cycling performances of $Fe_{(2-x)}Cr_xF_5\cdot H_2O$ nanocomposites ($x = 0\%, 3\%, 5\%, 7\%$) electrodes at 0.1 C rate within the voltage range of 1.0–4.0 V. (b) Rate capabilities of $Fe_{(2-x)}Cr_xF_5\cdot H_2O$ ($x = 0\%, 3\%, 5\%, 7\%$) cells.

densities. The undoped $Fe_2F_5\cdot H_2O$ shows an initial discharge capacity of 236 mAh g^{-1} at 0.1C. As the current density increased to 1C, the specific capacity decreases rapidly to 60 mAh g^{-1}, which is because of the serious electrochemical polarization of $Fe_2F_5\cdot H_2O$. Although a similar phenomenon can also be found for Cr-doped materials, the electrochemical polarization is smaller than undoped $Fe_2F_5\cdot H_2O$. For instance, the reversible capacities of $Fe_{1.95}Cr_{0.05}F_5\cdot H_2O$ remain as high as 328, 212, 166 and 141 mAh g^{-1} at 0.1, 0.2, 0.4 and 1 C, respectively, suggesting good rate capability of Cr-doped particles. Besides, When the current rate returns to 0.1 C after 20 cycles, the $Fe_{(2-x)}Cr_xF_5\cdot H_2O$ samples obtains the discharge capacity of about 135, 183, 232 and 204 mAh g^{-1} with the capacity retention of 57.0%, 65.2%, 65.7% and 70.6% respectively, indicating that the Cr-doped cathode material can still retain its structural integrity even at a high rate. The improved rate capability is usually believed to be associated with the introduction of Cr-doping and its unique open structure, which can be beneficial to transport of the electrolyte sodium ion, thus resulting in facilitating the intercalation process of sodium ions, enhancing sodium storage kinetics and shortening diffusion distance of Na^+ ions.

Fig. 6a shows the first three cyclic voltammogram (CV) curves of $Fe_{1.95}Cr_{0.05}F_5\cdot H_2O$ cathode at a scan rate of 0.2 mV s^{-1}. It can be seen that all redox peaks are consistent with the charge-discharge profiles (Fig. 4c) at 0.1C. In the first cathodic scan, two obvious reduction peaks at 2.5 and 1.2 V correspond to the two discharge plateaus respectively, and the low voltage peak positioned at 1.2 V may correspond to the chemical conversion reaction of fluoride cathode material. However, it is different from the next three cycles, where because of the rich surface defects of particles a high initial discharge capacity can be obtained (357 mAh g^{-1}). Moreover, starting from the second cycles, a pair of oxidation and reduction peaks located at 2.6 and 2.0 V can be observed, which are ascribed to the intercalation of Na^+ into the $Fe_{1.95}Cr_{0.05}F_5\cdot H_2O$. In addition, as being clearly observed in Fig. 6b, the CV curves of $Fe_2F_5\cdot H_2O$ and $Fe_{1.95}Cr_{0.05}F_5\cdot H_2O$ in second cycle dispaly the similar shape with a pair of redox peaks, which indicate that they have similar electrochemical reaction process. The oxidation and reduction peaks correspond to the Na^+ extraction and insertion processes. The larger peak area in the CV is in accord with the higher capacity of the respective samples, therefore $Fe_{1.95}Co_{0.05}F_5\cdot H_2O$ can provide a larger capacity. Besides, the redox peaks of $Fe_2F_5\cdot H_2O$ are detected at 2.66 V and 1.88 V, and the potential interval (ΔE_p) is 0.78 V, suggesting an acute polarization behavior. By comparison, the oxidation and reduction peaks of $Fe_{1.95}Cr_{0.05}F_5\cdot H_2O$ are positioned at 2.58 V and 1.97 V, and the ΔE_p is only 0.61 V, which is much smaller than that of $Fe_2F_5\cdot H_2O$. Usually, the smaller ΔE_p implies a smaller electrochemical polarization and a better cycling stability [25]. This is a good match with the charge-discharge and cycling curves, as shown in Fig. 4a, c.

As we all known, the mechanism of sodium storage of FeF_3 can be expressed as follows:

$$Na^+ + e^- + FeF_3 = NaFeF_3\ (4.0–2.0\ V) \quad (1)$$

$$2Na^+ + 2e^- + NaFeF_3 = 3NaF + Fe\ (2.0–1.0\ V) \quad (2)$$

During the discharge process, Na^+ is inserted into the crystal structure and Fe^{3+} was reduced to Fe^{2+} in the voltage range of 4.0–2.0 V, occurring the intercalation reactions as shown in Equation (1). In the next voltage range of 2.0–1.0 V, Fe^{2+} was reduced to Fe^0, occurring the conversion reactions as shown in Equation (2) [43]. Similarly, $Fe_2F_5\cdot H_2O$ also involves two kinds mechanism of intercalation and conversion according to the charge/discharge curves shown in Fig. 4. To study the phase transformation upon sodiation/desodiation, the HRTEM and SAED images were shown in Fig. 6c–f and the insert of Fig. 6e. Fig. 6c shows the HRTEM images of $Fe_{1.95}Cr_{0.05}F_5\cdot H_2O$ discharged to 1.0 V. The nanodomains with the lattice stripe corresponding to (111) and (002) are assigned to NaF and Fe respectively, indicating the presence of the conversion reaction [44]. When the $Fe_{1.95}Cr_{0.05}F_5\cdot H_2O$ electrode is recharged to 4.0 V, NaF and Fe were still detected and the lattice stripes of FeF_3 can also be found, as shown in Fig. 6d. Therefore, it can be inferred that Na^+ are extracted successfully from the material, and the conversion reaction is not completely reversible, which thus influences the cycle stability of electrode. The HRTEM images of the fully charged $Fe_{1.95}Cr_{0.05}F_5\cdot H_2O$ electrode after 100 cycles are shown in Fig. 6e. The crystalline phase and the amorphous phase coexist in the material. Furthermore, it can be clearly seen from the regional magnified image shown in Fig. 6f that the core region is remained the crystal phase while the edge region is converted to amorphous phase, indicating that the reaction upon sodiation/desodiation involves two kinds mechanism of intercalation and conversion.

To further determine structural changes during sodiation/desodiation, the XRD patterns of $Fe_{1.95}Cr_{0.05}F_5\cdot H_2O$ electrodes at different potential during the first cycle process are shown in

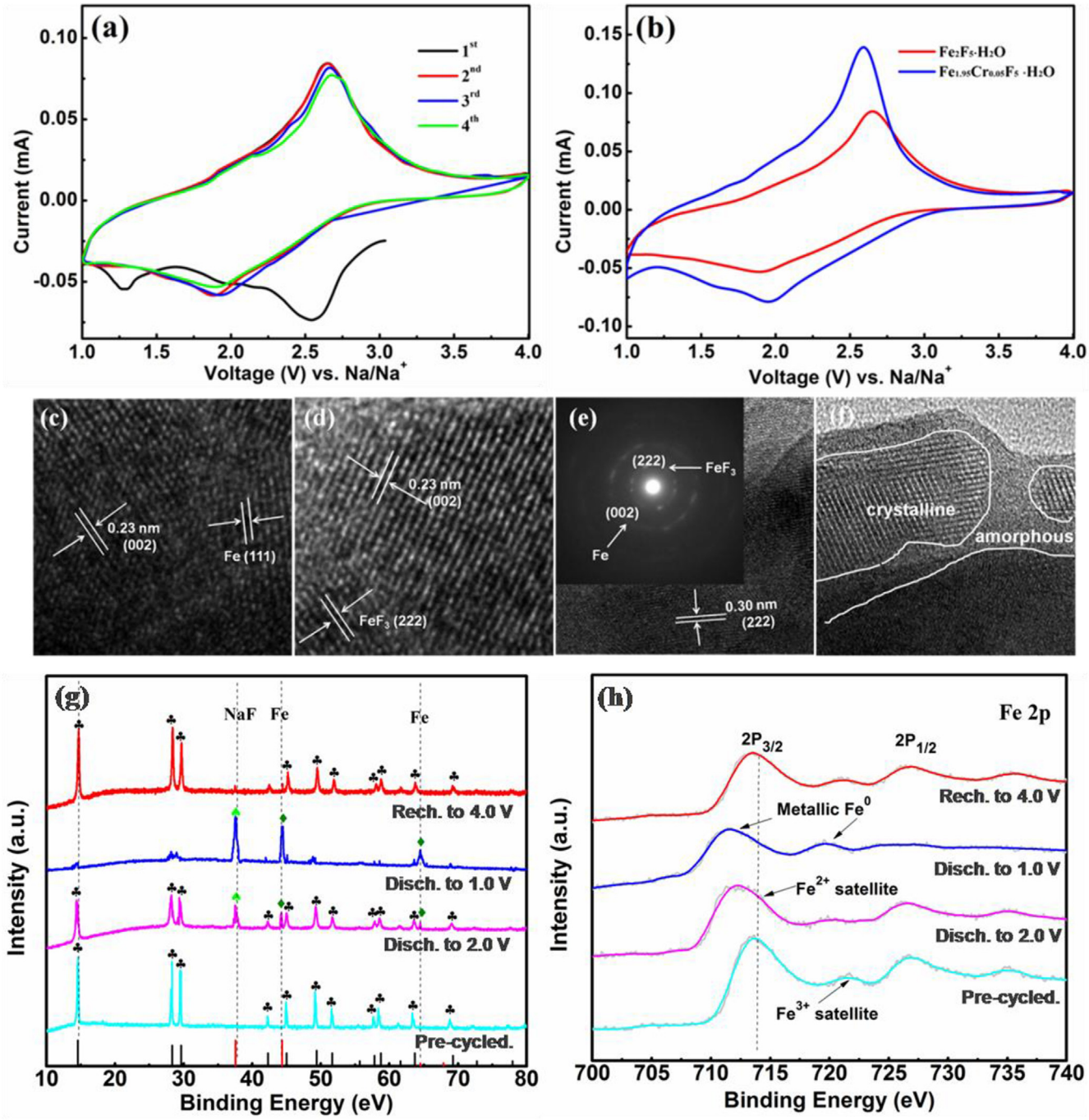

Fig. 6. (a) Cyclic voltammograms of $Fe_{1.95}Cr_{0.05}F_5 \cdot H_2O$ composite during the first 4 cycles at a scan rate of 0.2 mV s^{-1} within the voltage range of 1.0–4.0 V, (b) Cyclic voltammograms of $Fe_2F_5 \cdot H_2O$ and $Fe_{1.95}Cr_{0.05}F_5 \cdot H_2O$ at a scan rate of 0.2 mV s^{-1}. The HRTEM images of $Fe_{1.95}Cr_{0.05}F_5 \cdot H_2O$ (c) discharged to 1.0 V and (d) recharged to 4.0 V. (e) The HRTEM image of the fully charged $Fe_{1.95}Cr_{0.05}F_5 \cdot H_2O$ electrode after 100 cycles and (f) its regional magnified image. (g) XRD patterns and (h) XPS spectra of $Fe_{1.95}Cr_{0.05}F_5 \cdot H_2O$ electrodes at various reaction stages of the first cycle.

Fig. 6g. During the discharge process to 2.0 V, the intensity of typical diffraction peaks (marked with the plum-flower-type black symbol) are gradually decreased owing to the stress and disorder of crystal structures caused by the Na^+ intercalation into $Fe_2F_5 \cdot H_2O$ cavities. It is noteworthy that some new peaks at 37.60, 44.35 and 64.53° can also be observed, which can be well-indexed to NaF (marked with the peach-type green symbol) and Fe metal (marked with the peach-type olive symbol), suggesting the onset of the conversion reaction from Fe^{2+} to Fe^0. Furthermore, as the Na insertion proceeds, a continuous shift towards lower 2θ angles indicates a solid-solution behavior of the Na^+ insertion into large-size tunnels. When the $Fe_{1.95}Cr_{0.05}F_5 \cdot H_2O$ electrode is discharged to 1.0 V, the typical diffraction peaks almost disappeared, suggesting the transformation of $Fe_{1.95}Cr_{0.05}F_5 \cdot H_2O$ towards amorphous phase. Meanwhile, the intensity of diffraction peaks of NaF and Fe are increased since the NaF and Fe products are continuously produced. Once sodium is removed from the tunnels during the recharge process to 4.0 V, most diffraction peaks of the $Fe_{1.95}Cr_{0.05}F_5 \cdot H_2O$ are almost restored as the pre-cycled electrode. However, weak diffraction peaks attributing to NaF and Fe still

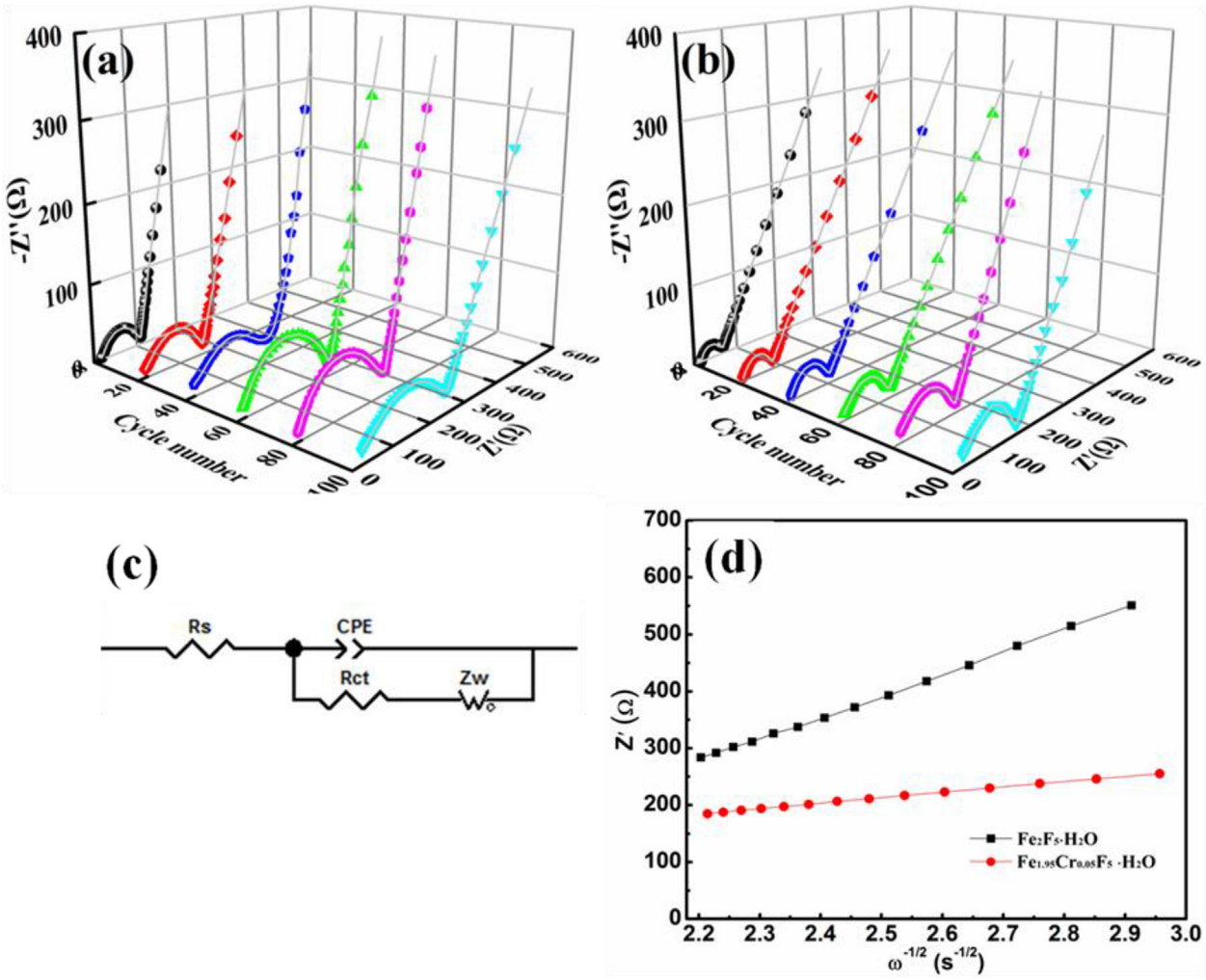

Fig. 7. Three-dimensional Nyquist plots measured for (a) $Fe_2F_5 \cdot H_2O$ and (b) $Fe_{1.95}Cr_{0.05}F_5 \cdot H_2O$ after cycling for different cycles at 0.1 C. (c) the equivalent circuit model. (d) The Z′ vs. $\omega^{-1/2}$ plots at low frequency region.

exist, demonstrating small irreversible capacity of $Fe_{1.95}Cr_{0.05}F_5 \cdot H_2O$. In addition, XPS spectra obtained from different voltage during charge/discharge process are used to detect the chemical state variation of $Fe_{1.95}Cr_{0.05}F_5 \cdot H_2O$ electrodes, as shown in Fig. 6h. During the discharging process, the Fe 2p XPS peaks of the $Fe_{1.95}Cr_{0.05}F_5 \cdot H_2O$ electrode systematically shift to lower energy during the discharge process because of the reduce reaction of Fe^{3+} actuated by Na. Comparing to the pre-cycled sample, all satellite peaks of Fe^{3+} almost disappeared and the intensity of Fe^{2+} peaks increase, revealing the Fe^{3+} reducing to Fe^{2+}. When the $Fe_{1.95}Cr_{0.05}F_5 \cdot H_2O$ electrode further discharged to 1.0 V, binding energy peaks of Fe $2p_{3/2}$ and Fe $2p_{1/2}$ locating at 710.40 and 719.41 can be ascribed to formation of Fe metal, which accords well with ex-situ XRD results. During the following charge process to 4.0 V, a reversed tendency of the shift in the XPS spectra is observed and the intensity of the peaks is similar to the pre-cycled sample, which reveals the oxidation of Fe upon the extraction of Na^+. All above results indicate the considerable reversibility of the $Fe_{1.95}Cr_{0.05}F_5 \cdot H_2O$ during the Na ion intercalation/de intercalation process.

Furthermore, the electrochemical impedance spectroscopy (EIS) measurements for $Fe_2F_5 \cdot H_2O$ and $Fe_{1.95}Cr_{0.05}F_5 \cdot H_2O$ were performed for different cycles as shown Fig. 7. The EIS pattern is composed of one high-frequency semicircle and a sloping line in low-frequency region. The semicircle is associated with the charge transfer resistance (R_{ct}) reflecting the reaction kinetics of the electrode reaction and the sloping line represents the diffusion impedance (Z_W), which is attributed to the diffusion of Na^+ into the solid matrix. The equivalent circuit model in Fig. 7c the electrolyte resistance R_s represents the total impedance of the electrode material and electrolyte. The fitting results are listed in Table 3, which are well matched to the experimental data described in Fig. 7a and b. It can be known from Table 3 that the R_s values of $Fe_{1.95}Cr_{0.05}F_5 \cdot H_2O$ at different cycles are apparently less than that of $Fe_2F_5 \cdot H_2O$, suggesting the conductivity of $Fe_{1.95}Cr_{0.05}F_5 \cdot H_2O$ after Cr-doping has well improved. In addition, the R_{ct} value of $Fe_2F_5 \cdot H_2O$ is 104 Ω after first cycle, but this value increases to 305 Ω after 100 cycles. On the contrary, the R_{ct} of $Fe_{1.95}Cr_{0.05}F_5 \cdot H_2O$ are 62 Ω, and 168 Ω after 1 and 100 cycles. The R_{ct} of $Fe_{1.95}Cr_{0.05}F_5 \cdot H_2O$ is less than that of $Fe_2F_5 \cdot H_2O$, indicating that the $Fe_{1.95}Cr_{0.05}F_5 \cdot H_2O$ composite has a higher electrochemical activity, less polarization and better electrochemical performance than $Fe_2F_5 \cdot H_2O$. In order to evaluate the influence of Cr-doping on the diffusion of Na^+, the diffusion coefficient of sodium ion (D_{Na}^+) are calculated as follows [45]:

Table 3
R_s and R_{ct} values of $Fe_2F_5\cdot H_2O$ and $Fe_{1.95}Cr_{0.05}F_5\cdot H_2O$ after different cycles.

Samples	$Fe_2F_5\cdot H_2O$						$Fe_{1.95}Cr_{0.05}F_5\cdot H_2O$					
	1st	20th	40th	60th	80th	100th	1st	20th	40th	60th	80th	100th
R_s (Ω)	13.0	18.0	14.5	15.3	21.8	22.5	9.7	12.1	13.0	16.9	19.3	24.3
R_{ct} (Ω)	104	156	198	241	284	305	62	81	105	127	155	160

$$DNa^+ = \frac{R^2T^2}{2A^2n^4F^4C^2\sigma^2} \quad (3)$$

$$C = \frac{n}{V} = \frac{m/M}{V} = \frac{\rho V/M}{V} = \frac{\rho}{M} \quad (4)$$

A is the surface area of electrode, C is the molar concentration of Na^+ in the electrode and can be calculated from the molecular weight (M) and the density (ρ) of the materials [46]. F is Faraday constant, T is the absolute temperature, R is the ideal gas constant, n is the number of electron per molecule in the reaction and σ is the Warburg coefficient related to Z':

$$Z' = R_s + R_{ct} + \sigma\omega^{-1/2} \quad (5)$$

where ω is the angular frequency in the low frequency region. The linear relationship between Z′ and $\omega^{-1/2}$ of $Fe_2F_5\cdot H_2O$ and $Fe_{1.95}Cr_{0.05}F_5\cdot H_2O$ in the low-frequency region is shown in Fig. 7d. It can be known from calculation that the Na^+ diffusion coefficients of $Fe_2F_5\cdot H_2O$ after 100 cycles is $9.57\times10^{-17}\,m^2\,s^{-1}$, which demonstrated that the $Fe_2F_5\cdot H_2O$ electrode has a relatively lower diffusivity, presumably owing to serious polarization and structural changes. Nevertheless, the corresponding Na^+ diffusion coefficients of $Fe_{1.95}Co_{0.05}F_5\cdot H_2O$ after 100 cycles is $7.21\times10^{-15}\,m^2\,s^{-1}$. Obviously, the Na^+ diffusion coefficients of $Fe_{1.95}Co_{0.05}F_5\cdot H_2O$ is clearly higher than one of the $Fe_2F_5\cdot H_2O$. Therefore, above results indicate that Cr-doping can effectively facilitate the insertion/deintercalation process of sodium ions and enhance sodium storage kinetics, and thus improving its electrochemical performances.

4. Conclusions

The Cr-doped $Fe_2F_5\cdot H_2O$ cathode materials for NIBs with open framework structure were successfully prepared by an IL based assisted method. The effects of Cr^{3+} doping on the structure, morphology, and electrochemical characteristics of $Fe_2F_5\cdot H_2O$ were investigated. Cr is successfully doped into $Fe_2F_5\cdot H_2O$ crystal structure without varying its structure fundamentally, but Cr doping can cause a slight decrease in crystalline size. Among all of the samples, the $Fe_{1.95}Cr_{0.05}F_5\cdot H_2O$ sample exhibited excellent electrochemical property, delivering maximum discharge capacities of 328, 212, 166 and 147 mAh g^{-1} at rates of 0.1, 0.3, 0.5 and 1 C. Meanwhile, the discharge capacity of $Fe_{1.95}Cr_{0.05}F_5\cdot H_2O$ retains 171 mAh g^{-1} after 100 cycles at 0.1 C. Especially, even at high rate of 1 C, it can still exhibit a high discharge capacity of 147 mAh g^{-1}. The lower electrode polarization and the improvement of dynamic behavior can usually be ascribed to the introduction of the high oxygen affinity Cr element, which leads to an increase in electronic conductivity of material. Therefore, Cr doping may be a feasible and effective methodology to overcome the intrinsic drawbacks of iron fluoride as a high performance cathode material of NIBs.

Acknowledgements

This work is supported financially by the National Natural Science Foundation of China under project No. 51272221, Key Project of Strategic New Industry of Hunan Province under project No. 2016GK4005 and 2016GK4030.

References

[1] H. Kim, H. Kim, Z. Ding, M.H. Lee, K. Lim, G. Yoon, K. Kang, Recent progress in electrode materials for sodium-ion batteries, Adv. Energy Mater 6 (2016), 1600943.
[2] S.P. Ong, V.L. Chevrier, G. Hautier, A. Jain, C. Moore, S. Kim, X. Ma, G. Ceder, Voltage, stability and diffusion barrier differences between sodium-ion and lithium-ion intercalation materials, Energy Environ. Sci. 4 (2011) 3680–3688.
[3] N. Yabuuchi, M. Kajiyama, J. Iwatate, H. Nishikawa, S. Hitomi, R. Okuyama, R. Usui, Y. Yamada, S. Komaba, P2-type Nax[Fe1/2Mn1/2]O2 made from earth-abundant elements for rechargeable Na batteries, Nat. Mater. 11 (2012) 512–517.
[4] Z. Jian, L. Zhao, H. Pan, Y.S. Hu, H. Li, W. Chen, L. Chen, Carbon coated $Na_3V_2(PO_4)_3$ as novel electrode material for sodium ion batteries, Electrochem. Commun. 14 (2012) 86–89.
[5] P. Barpanda, G. Oyama, S. Nishimura, S.C. Chung, A. Yamada, A 3.8-V earth-abundant sodium battery electrode, Nat. Commun. 5 (2014) 4358.
[6] J. Song, L. Wang, Y.H. Lu, J. Liu, B.K. Guo, P.H. Xiao, J.J. Lee, X.Q. Yang, G. Henkelman, J.B. Goodenough, Removal of interstitial H_2O in hexacyanometallates for a superior cathode of a sodium-ion battery, J. Am. Chem. Soc. 137 (2015) 2658.
[7] P. Moreau, D. Guyomard, J. Gaubicher, F. Boucher, Structure and stability of sodium intercalated phases in olivine $FePO_4$, Chem. Mater. 22 (2010) 4126–4128.
[8] Y. Han, J. Hu, C. Yin, Y. Zhang, J. Xie, D. Yin, C. Li, Iron-based fluorides of tetragonal tungsten bronze structure as potential cathodes for Na-ion batteries, J. Mater. Chem. 4 (2016) 7382–7389.
[9] G.G. Amatucci, N. Pereira, Fluoride based electrode materials for advanced energy storage devices, J. Fluorine Chem. 128 (2007) 243–262.
[10] M. Armand, J.M. Tarascon, Building better batteries, Nature 451 (2008) 652–657.
[11] F. Wu, C. Wu, New secondary batteries and their key materials based on the concept of multi-electron reaction, Chin. Sci. Bull. 59 (2014) 3369–3376.
[12] L.P. Ding, X.Y. Kuang, P. Shao, M.M. Zhong, Y. Zhao, Formation and properties of iron-based magnetic superhalogens: a theoretical study, J. Chem. Phys. 139 (2013) 10430401–10430410.
[13] G. Ferey, M. Leblanc, R.D. Pape, Crystal structure of the ordered pyrochlore $NH_4Fe^{II}Fe^{III}F_6$ structural correlations with $Fe_2F_5\cdot 2H_2O$ and its dehydration product $Fe_2F_5\cdot 2H_2O$, J. Solid State Chem. 40 (1981) 1–7.
[14] C. Li, C. Yin, L. Gu, R.E. Dinnebier, X. Mu, P.A. van Aken, J. Maier, An $FeF_3\cdot 0.5H_2O$ polytype: a microporous framework compound with intersecting tunnels for Li and Na batteries, J. Am. Chem. Soc. 135 (2013) 11425–11428.
[15] M. Jiang, X. Wang, S. Wei, Y. Shen, H. Hu, An ionic-liquid-assisted approach to synthesize a reduced graphene oxide loading iron-based fluoride as a cathode material for sodium-ion batteries, J. Alloys. Compd 670 (2016) 362–368.
[16] M. Jiang, X. Wang, H. Hu, Y. Fu, S. Wei, Y. Shen, In situ growth and performance of spherical $Fe_2F_5\cdot H_2O$ nanoparticles in multi-walled carbon nanotube network matrix as cathode material for sodium ion batteries, J. Power Sources 316 (2016) 170–175.
[17] F. Badway, N. Pereira, F. Cosandey, G.G. Amatucc, Carbon-metal fluoride nanocomposites: structure and electrochemistry of FeF_3-C, J. Electrochem. Soc. 150 (2003) A1209–A1218.
[18] G. Ali, S.H. Oh, S.Y. Kim, J.Y. Kim, B.W. Cho, K.Y. Chung, An open-framework iron fluoride and reduced graphene oxide nanocomposite as a high-capacity cathode material for Na-ion batteries, J. Mater. Chem. 3 (2015) 10258–10266.
[19] G. Ali, J.H. Lee, B.W. Cho, K.-W. Nam, D. Ahn, W. Chang, S.H. Oh, K.Y. Chung, Probing the sodiation-desodiation reactions in nano-sized iron fluoride cathode, Electrochim. Acta 191 (2016) 307–316.
[20] C. Li, L. Gu, J. Tong, J. Maier, Carbon nanotube wiring of electrodes for high-rate lithium batteries using an imidazolium-based ionic liquid precursor as dispersant and binder: a case study on iron fluoride nanoparticles, ACS Nano 5 (2011) 2930–2938.
[21] K.-C. Jiang, X.-L. Wu, Y.-X. Yin, J.-S. Lee, J. Kim, Y.-G. Guo, Superior hybrid cathode material containing lithium-excess layered material and graphene for lithium-ion batteries, ACS Appl. Mater. Interfaces 4 (2012) 4858–4863.
[22] R. Yu, X. Wang, Y. Fu, L. Wang, S. Cai, M. Liu, B. Lu, G. Wang, D. Wang, Q. Ren, X. Yang, Effect of magnesium doping on properties of lithium-rich layered

oxide cathodes based on a one-step co-precipitation strategy, J. Mater. Chem. 4 (2016) 4941–4951.
[23] Z. Yang, Z. Zhang, Y. Yuan, Y. Huang, X. Wang, X. Chen, S. Wei, First-principles study of Ti doping in $FeF_3 \cdot 0.33H_2O$, Curr. Appl. Phys. 16 (2016) 905–913.
[24] L. Liu, M. Zhou, L. Yi, H. Guo, J. Tan, H. Shu, X. Yang, Z. Yang, X. Wang, Excellent cycle performance of Co-doped FeF_3/C nanocomposite cathode material for lithium-ion batteries, J. Mater. Chem. 22 (2012) 17539–17550.
[25] Y. Bai, X. Zhou, Z. Jia, C. Wu, L. Yang, M. Chen, H. Zhao, F. Wu, G. Liu, Understanding the combined effects of microcrystal growth and band gap reduction for $Fe_{(1-x)}Ti_xF_3$ nanocomposites as cathode materials for lithium-ion batteries, Nano Energy 17 (2015) 140–151.
[26] M.-H. Cao, Y. Wang, Z. Shadike, J.-L. Yue, E. Hu, S.-M. Bak, Y.-N. Zhou, X.-Q. Yang, Z.-W. Fu, Suppressing chromium disproportion reaction in O_3-type layered cathode material for high capacity sodium-ion batteries, J. Mater. Chem. 5 (2017) 5442–5448.
[27] M.J. Aragón, P. Lavela, G.F. Ortiz, J.L. Tirado, Benefits of chromium substitution in $Na_3V_2(PO_4)_3$ as a potential candidate for sodium-ion batteries, ChemElectroChem 2 (2015) 995–1002.
[28] H. Zhuo, X. Wang, A. Tang, Z. Liu, S. Gamboa, P.J. Sebastian, The preparation of $NaV_{1-x}Cr_xPO_4F$ cathode materials for sodium-ion battery, J. Power Sources 160 (2006) 698–703.
[29] A. Trueba, J.M. García-Lastra, P. Garcia-Fernandez, J.A. Aramburu, M.T. Barriuso, M. Moreno, Cr^{3+}-doped fluorides and oxides: role of internal fields and limitations of the Tanabe-Sugano approach, J. Phys. Chem. 115 (2011) 13399–13406.
[30] C. Li, C. Yin, L. Gu, R.E. Dinnebier, X. Mu, P.A. van Aken, J. Maier, An FeF3·0.5H2O polytype: a microporous framework compound with intersecting tunnels for Li and Na batteries, J. Am. Chem. Soc. 135 (2013) 11425–11428.
[31] H. An, Y. Wang, X. Wang, L. Zheng, X. Wang, L. Yi, L. Bai, X. Zhang, Polypyrrole/carbon aerogel composite materials for supercapacitor, J. Power Sources 195 (2010) 6964–6969.
[32] M. Jiang, X. Wang, Y. Shen, H. Hu, Y. Fu, X. Yang, New iron-based fluoride cathode material synthesized by non-aqueous ionic liquid for rechargeable sodium ion batteries, Electrochim. Acta 186 (2015) 7–15.
[33] J.F. Moulder, W.F. Stickle, P.E. Sobol, K.D. Bomben, in: J. Chastain (Ed.), Handbook of X-ray photoelectron spectroscopy, Perkin-Elmer Corporation, Eden Prairie, MN, 1992.
[34] B. Dong, H.Q. Zhang, A. Kong, Y.Y. Kong, F. Yang, Y.K. Shan, Synthesis of urchin-like FeF_2 nanoarchitectures and their conversion into three-dimensional urchin-like mesoporous α-Fe_2O_3 nanoarchitectures for methane activation, Eur. J. Inorg. Chem. 2014 (2014) 4779–4787.
[35] B. Peebles, A. Nagy, W.J. Waldman, P.K. Dutta, Fenton activity and cytotoxicity studies of iron-loaded carbon particles, Environ. Sci. Technol. 4 (2010) 6887–6892.
[36] C. Wu, Z. Wang, F. Wu, L. Chen, X. Huang, Spectroscopic studies on cation-doped spinel $LiMn_2O_4$ for lithium ion batteries, Solid State Ion 144 (2001) 277–285.
[37] C. Wu, F. Wu, L. Chen, X. Huang, X-ray diffraction and X-ray photoelectron spectroscopy analysis of Cr-doped spinel $LiMn_2O_4$ for lithium ion batteries, Solid State Ion 152–153 (2002) 335–339.
[38] Y.L. Shi, M.F. Shen, S.D. Xu, Q.C. Zhuang, L. Jiang, Y.H. Qiang, Electrochemical impedance spectroscopy investigation of the FeF_3/C cathode for lithium-ion batteries, Solid State Ion 222 (2012) 23–30.
[39] C. Wu, Y. Bai, F. Wu, Fourier-transform infrared spectroscopic studies on the solid electrolyte interphase formed on Li-doped spinel Li1.05Mn1.96O4 cathode, J. Power Sources 189 (2009) 89–94.
[40] Y.-L. Shi, M.-F. Shen, S.-D. Xu, X.-Y. Qiu, L. Jiang, Y.-H. Qiang, Q.-C. Zhuang, S.-G. Sun, Electrochemical impedance spectroscopic study of the electronic and ionic transport properties of NiF2/C composites, Int. J. Electrochem. Sci. 6 (2011) 3399–3415.
[41] D-l Ma, H-g Wang, Y. Li, D. Xu, S. Yuan, X-l Huang, X-b Zhang, Y. Zhang, In situ generated FeF3 in homogeneous iron matrix toward high-performance cathode material for sodium-ion batteries, Nano Energy 10 (2014) 295–304.
[42] L. Li, F. Meng, S. Jin, High-capacity lithium-ion battery conversion cathodes based on iron fluoride nanowires and insights into the conversion mechanism, Nano Lett. 12 (2012) 6030–6037.
[43] J. Hu, Y. Zhang, D. Cao, C. Li, Dehydrating bronze iron fluoride as high capacity conversion cathode for lithium batteries, J. Mater. Chem. 4 (2016) 16166–16174.
[44] G. Ali, S.H. Oh, S.Y. Kim, J.Y. Kim, B.W. Cho, K.Y. Chung, An open-framework iron fluoride and reduced graphene oxide nanocomposite as a high-capacity cathode material for Na-ion batteries, J. Mater. Chem. 3 (2015) 10258–10266.
[45] F. Gao, Z. Tang, Kinetic behavior of LiFePO4/C cathode material for lithium-ion batteries, Electrochim. Acta 53 (2008) 5071–5075.
[46] X. Wang, H. Hao, J. Liu, T. Huang, A. Yu, A novel method for preparation of macroposous lithium nickel manganese oxygen as cathode material for lithium ion batteries, Electrochim. Acta 56 (2011) 4065–4069.